



## Quark phases in neutron stars consistent with implications from NICER observations

Y. Yamamoto <sup>1,\*</sup>, N. Yasutake,<sup>2</sup> and Th. A. Rijken <sup>3,1</sup>

<sup>1</sup>*RIKEN Nishina Center, 2-1 Hirosawa, Wako, Saitama 351-0198, Japan*

<sup>2</sup>*Department of Physics, Chiba Institute of Technology, 2-1-1 Shibazono Narashino, Chiba 275-0023, Japan*

<sup>3</sup>*IMAPP, Radboud University, Nijmegen, The Netherlands*



(Received 7 June 2023; revised 18 August 2023; accepted 15 September 2023; published 26 September 2023)

The analyses of NICER data imply  $R_{2.0M_{\odot}} = 12.41_{-1.10}^{+1.00}$  km and  $R_{1.4M_{\odot}} = 12.56_{-1.07}^{+1.00}$  km, indicating the lack of significant variation of the radii from  $1.4M_{\odot}$  to  $2.0M_{\odot}$ . This feature cannot be reproduced by hadronic matter due to the softening of equation of state (EoS) by hyperon mixing, indicating the possible existence of quark phases in neutron-star interiors. Two models are used for quark phases: In the quark-hadron transition (QHT) model, quark deconfinement phase transitions from a hadronic-matter EoS are taken into account so as to give reasonable mass-radius ( $MR$ ) curves by adjusting the quark-quark repulsions and the density dependence of the effective quark mass. In the quarkyonic model, the degrees of freedom inside the Fermi sea are treated as quarks, and neutrons exist at the surface of the Fermi sea, where  $MR$  curves are controlled mainly by the thickness of neutron Fermi layer. The QHT and quarkyonic EoSs can be adjusted so as to reproduce radii, tidal deformabilities, pressure, and central densities inferred from the NICER analysis better than the nucleonic matter EoS, demonstrating the clear impacts of quark phases. Then, the maximum mass for the quarkyonic-matter EoS is considerably larger than that for the QHT-matter EoS.

DOI: [10.1103/PhysRevC.108.035811](https://doi.org/10.1103/PhysRevC.108.035811)

### I. INTRODUCTION

In studies of neutron stars (NSs), the fundamental role is played by the equation of state (EoS) for neutron star matter. Massive neutron stars with masses over  $2M_{\odot}$  have been reliably established by the observations of NSs J1614 – 2230 [1], J0348 + 0432 [2], J0740 + 6620 [3], and J0952 – 0607 [4]. The radius information of NSs has been obtained for the massive NS PSR J0740+6620, with  $2M_{\odot}$  and  $1.4M_{\odot}$  NS radii, denoted as  $R_{2M_{\odot}}$  and  $R_{1.4M_{\odot}}$ , from the analyses of the x-ray data taken by the Neutron Star Interior Composition Explorer (NICER) and the X-ray Multi-Mirror (XMM-Newton) observatory. The analysis of Miller *et al.* gives  $R_{2.08M_{\odot}} = 12.35 \pm 0.75$  km and  $R_{1.4M_{\odot}} = 12.45 \pm 0.65$  km [5]. The analysis of Riley gives  $R_{2.08M_{\odot}} = 12.39_{-0.98}^{+1.30}$  km and  $R_{1.4M_{\odot}} = 12.33_{-0.81}^{+0.76}$  km [6]. Legred *et al.* investigated these measurement's implications for the EoSs, employing a non-parametric EoS model based on Gaussian processes and combining information from other x-ray and gravitational wave observations [7].

The purpose of this paper is to demonstrate that the radius information of massive NSs give important constraints on the neutron-star EoSs. In our EoS analysis, the following neutron-star radii are adopted as critical values to be reproduced:

$$\begin{aligned} R_{2.0M_{\odot}} &= 12.41_{-1.10}^{+1.00} \text{ km}, \\ R_{1.4M_{\odot}} &= 12.56_{-1.07}^{+1.00} \text{ km}, \end{aligned} \quad (1.1)$$

with maximum mass  $M_{\text{max}}/M_{\odot} = 2.21_{-0.21}^{+0.31}$ , which is given by the analysis by Legred *et al.* [7]. The median values of  $R_{2M_{\odot}}$  and  $R_{1.4M_{\odot}}$  in the three Refs. [5–7] are only a few hundred meters apart from each other. We set the fitting accuracy to a few hundred meters in our analysis for  $R_{2M_{\odot}}$  and  $R_{1.4M_{\odot}}$ . Then, the EoSs obtained from our analysis are not changed, even if the set of  $R_{2M_{\odot}}$  and  $R_{1.4M_{\odot}}$  in [5] or [6] is used as the criterion instead of Eq. (1.1) or all three sets in [5–7] are used. The key feature found commonly in the three sets is the small variation of radii from  $1.4M_{\odot}$  to  $2M_{\odot}$ , namely  $R_{2M_{\odot}} \approx R_{1.4M_{\odot}}$ . The reason why the result in [7] is used in our present analysis is because they present the inferred values of maximum masses, radii, tidal deformabilities, pressure, and central densities obtained from their analysis. These quantities can be compared with our corresponding results, by which the features of our EoSs are revealed in detail.

The hyperon mixing in neutron-star matter brings about a remarkable softening of the EoS, and the maximum mass is reduced to a value far less than  $2M_{\odot}$ . The EoS softening is caused by changing of high-momentum neutrons at Fermi surfaces to low-momentum hyperons via strangeness nonconserving weak interactions overcoming rest masses of hyperons. In order to derive EoSs for massive NSs, it is necessary to solve this “hyperon puzzle in neutron stars.” Possible mechanisms have been proposed:

- (i) more repulsive hyperon-hyperon interactions in relativistic mean field (RMF) models driven by vector mesons exchanges [8–11],
- (ii) repulsive hyperonic three-body forces [12–19],
- (iii) appearance of other hadronic degrees of freedom, such as  $\Delta$  isobars [20] or meson condensates [21–25],

\*yamamoto@tsuru.ac.jp

- (iv) existence of quark phases in high-density regions [26–36].

It should be noted that the criterion for NS radii, Eq. (1.1), is stricter than the condition of  $M_{\max} > 2M_{\odot}$  only to solve the “puzzle,” and the above mechanisms need to be reinvestigated under this stricter condition.

One of the approaches to (ii) is to assume that three-nucleon repulsions (TNRs) [37] work universally among every kind of baryon as three-baryon repulsions (TBRs) [12]. In [14–16], the multi-Pomeron exchange potential (MPP) was introduced as a model of universal repulsions among three and four baryons on the basis of the extended soft core (ESC) baryon-baryon interaction model developed by two of the present authors (T.R. and Y.Y.) and by Nagels [38–40]. In the case of this special modeling for hyperonic three-body repulsions, the EoS softening by hyperon mixing is not completely recovered by the above universal repulsions, and the maximum masses become not so large even if universal many-body repulsions increase. As a result, the maximum masses for the hyperonic-matter EoS cannot be over  $2M_{\odot}$ , as found in [14–16]: It is difficult that criterion (1.1) is realized by this modeling of hadronic-matter EoSs. A simple way to avoid the strong softening of the EoS by hyperon mixing is to assume that  $\Lambda NN$  repulsions are stronger than  $NNN$  repulsions with neglect of  $\Sigma^{-}$  mixing [17].

In this paper, we focus on the mechanism (iv). It is possible to solve the “hyperon puzzle” by taking account of quark deconfinement phase transitions from a hadronic-matter EoS to a sufficiently stiff quark-matter EoS in neutron-star interiors, namely by studying hybrid stars having quark matter in their cores, where repulsive effects in quark phases are needed to result in massive stars over  $2M_{\odot}$ . In the Nambu–Jona-Lasinio (NJL) model, for instance, repulsions to stiffen EoSs are given by vector interactions. Then, it is known well that quark-hadron phase transitions should be crossover or at most weak first order, because strong first-order transitions soften EoSs remarkably in order to obtain stiff EoSs. In [35], the authors derived a new EoS within the quark-hadron crossover (QHC) framework (three-windows model) so as to reproduce  $R_{2.1M_{\odot}} \approx R_{1.4M_{\odot}} \approx 12.4$  km. Here, the small variation of radii indicates that the pressure grows rapidly while changes in energy density are modest, producing a peak in the speed of sound [35]. In their QHC framework, the EoSs in the quark-hadron mixed region of  $1.5\rho_0$ – $3.5\rho_0$ , playing a decisive role for the resulting  $MR$  curves, are given by the interpolating functions phenomenologically. Then, it is meaningful to study other modeling for phase transitions, in which the mixed regions are modeled explicitly. We investigate how the criterion (1.1) can be realized in the case of using the EoS derived from our quark-hadron transition (QHT) model for neutron-star matter in the Bruecner-Hartree-Fock (BHF) framework [36], which is different from the three-windows model. Here, the quark-matter EoS is derived from the two-body quark-quark ( $QQ$ ) potentials, in which all parameters are on the physical backgrounds with no room for arbitrary changes: Our  $QQ$  potential is composed of meson-exchange, instanton exchange, one-gluon exchange and multi-Pomeron exchange potentials. Then, baryonic matter and quark matter are treated in the

common BHF framework, where quark-hadron transitions are treated on the basis of the Maxwell condition. In this paper, it is shown that the criterion (1.1) can be realized by our QHT model for neutron-star matter, as well as the QHC model [35], by adjusting the  $QQ$  repulsion to be strong enough and the quark-hadron transition density to be about  $2\rho_0$ .

In our QHT model the BHF framework is used for deriving the quark-matter EoS, which is not common. Our treatment for quark-hadron phase transitions is the same as that in [33], where the NJL model is adopted for quark matter under the mean field approximation. In spite of the difference between quark-matter models, their obtained  $MR$  curves are similar to ours in [36]. Therefore, it is considered that the same conclusions can be derived also by using their QHT model instead of ours.

Another type of quark phase in neutron-star interiors is given by the quarkyonic matter [41–48], where the degrees of freedom inside the Fermi sea are treated as quarks, and nucleons exist at the surface of the Fermi sea. The transition from hadronic-matter phase to the quarkyonic-matter phase is considered to be in second order. In the quarkyonic matter, the existence of free quarks inside the Fermi sea gives nucleons extra kinetic energy by pushing them to higher momenta, leading to increasing pressure. This mechanism to realize the criterion (1.1) is completely different from the QHT matter in which the essential roles for EoS stiffening are played by the  $QQ$  repulsions. Then, it is valuable to study the characteristic differences between neutron-star mass-radius ( $MR$ ) curves obtained from the QHT-matter EoS and quarkyonic-matter EoS.

This paper is organized as follows: In Sec. II, the hadronic-matter EoS (II A), the quark-matter EoS (II B), and the quarkyonic-matter EoS (II-C) are formulated on the basis of our previous works, where the BHF frameworks with our  $QQ$  potentials are adopted both for baryonic matter and quark (quarkyonic) matter. Transitions from hadron phases to quark matter (quarkyonic) phases are explained. In Sec. III A, the calculated results are shown for pressures, energy densities, and sound velocities. In Sec. III B, the  $MR$  curves of hybrid stars are obtained by solving the Tolmann-Oppenheimer-Volkoff (TOV) equation. In Sec. III C, the obtained values of maximum masses, radii, tidal deformabilities, pressure, and central densities are compared with those inferred from the NICER-data analysis. The conclusion of this paper is given in Sec. IV.

## II. MODELS OF NEUTRON-STAR MATTER

### A. Hadronic matter

The hadronic matter is defined as  $\beta$ -stable hyperonic nuclear matter including leptons, composed of  $n$ ,  $p^+$ ,  $\Lambda$ ,  $\Sigma^-$ ,  $e^-$ ,  $\mu^-$ . We recapitulate here the hadronic-matter EoS. In the BHF framework, the EoS is derived with use of the ESC baryon-baryon ( $BB$ ) interaction model [14–16].

As is well known, the nuclear-matter EoS is stiff enough to assure neutron-star masses over  $2M_{\odot}$ , if the strong three-nucleon repulsion (TNR) is taken into account. However, there appears a remarkable softening of the EoS by inclusion

of exotic degrees of freedom such as hyperon mixing. One of the ideas to avoid this ‘‘hyperon puzzle’’ is to assume that the many-body repulsions work universally for every kind of baryon [12]. In [14–16], the multi-Pomeron exchange potential MPP was introduced as a model of universal repulsions among three and four baryons. This was inspired by the multi-Reggeon model to describe CERN-ISR  $pp$  data [49]. The ESC work is mentioned in [38–40].

In [16] the authors proposed three versions of MPP (MPa,  $\text{MPa}^+$ , MPb), where MPa and  $\text{MPa}^+$  (MPb) include the three- and four-body (only three-body) repulsions. Their strengths are determined by analyzing the nucleus-nucleus scattering using the  $G$ -matrix folding model under the conditions that the saturation parameters are reproduced reasonably. The EoSs for MPa and  $\text{MPa}^+$  are stiffer than that for MPb, and maximum masses and radii of neutron stars obtained from MPa and  $\text{MPa}^+$  are larger than those from MPb. The important criterion for repulsive parts is the resulting neutron-star radii  $R$  for masses of  $1.4M_\odot$ : In the case of using MPb, we obtain  $R_{1.4M_\odot} \approx 12.4$  km, similar to the value in the criterion (1.1). On the other hand, we have  $R_{1.4M_\odot} \approx 13.3$  (13.6) km in the case of MPa ( $\text{MPa}^+$ ). In this paper, we adopt MPb as three-baryon repulsion: Our nuclear interactions are composed of two-body part  $V_{BB}$  and three-body part  $V_{BBB}$ , where  $V_{BB}$  and  $V_{BBB}$  are given by ESC and MPb, respectively. It is worthwhile to say that the three-nucleon repulsion in MPb is stronger than the corresponding one (UIX) in the standard model by Akmal, Pandharipande, and Ravenhall (APR) [37] giving rise to  $R_{1.4M_\odot} \approx 11.6$  km [50].

$BB$   $G$ -matrix interactions  $\mathcal{G}_{BB}$  are derived from  $BB$  bare interactions  $V_{BB}$  or  $V_{BB} + V_{BBB}$  [14]. They are given for each ( $BB'$ ,  $T$ ,  $S$ ,  $P$ ) state,  $T$ ,  $S$ , and  $P$  being isospin, spin, and parity in a two-body state, respectively, and represented as  $\mathcal{G}_{BB'}^{TSP}$ . The  $G$ -matrix interactions derived from  $V_{BB}$  and  $V_{BB} + V_{BBB}$  are called B1 and B2, respectively. In the quarkyonic model, we need only the neutron-neutron sectors,  $\mathcal{G}_{nn}^{SP}$ .

A single baryon potential is given by

$$\begin{aligned} U_B(k) &= \sum_{B'=n,p,\Lambda,\Sigma^-} U_B^{(B')}(k) \\ &= \sum_{B'=n,p,\Lambda,\Sigma^-} \sum_{k' < k_F^{(B')}} \langle kk' | \mathcal{G}_{BB'} | kk' \rangle \end{aligned} \quad (2.1)$$

with  $B = n, p, \Lambda, \Sigma^-$ . Here,  $\langle kk' | \mathcal{G}_{BB'} | kk' \rangle$  is a  $BB'$   $G$  matrix element in momentum space, which is derived from  $V_{BB}$  or ( $V_{BB} + V_{BBB}$ ), and  $k_F^{(B)}$  is the Fermi momentum of baryon  $B$ . In this expression, spin and isospin quantum numbers are implicit.

The baryon energy density is given by

$$\begin{aligned} \varepsilon_B &= \tau_B + \nu_B \\ &= g_s \int_0^{k_F^{(B)}} \frac{d^3k}{(2\pi)^3} \left\{ \sqrt{\hbar^2 k^2 + M_B^2} + \frac{1}{2} U_B(k) \right\}, \end{aligned} \quad (2.2)$$

where  $\tau_B$  and  $\nu_B$  are kinetic and potential parts of the energy density.

In  $\beta$ -stable hadronic matter composed of  $n, p, e^-, \mu^-, \Lambda,$  and  $\Sigma^-$ , equilibrium conditions are given as

(1) chemical equilibrium conditions,

$$\mu_n = \mu_p + \mu_e, \quad (2.3)$$

$$\mu_\mu = \mu_e, \quad (2.4)$$

$$\mu_\Lambda = \mu_n, \quad (2.5)$$

$$\mu_{\Sigma^-} = \mu_n + \mu_e, \quad (2.6)$$

(2) charge neutrality,

$$\rho_p = \rho_e + \rho_\mu + \rho_{\Sigma^-}, \quad (2.7)$$

(3) baryon number conservation,

$$\rho = \rho_n + \rho_p + \rho_\Lambda + \rho_{\Sigma^-}. \quad (2.8)$$

Expressions for  $\beta$ -stable nucleonic matter composed of  $n, p, e^-$ , and  $\mu^-$  are obtained by omitting hyperon sectors from the above expressions for  $\beta$ -stable baryonic matter.

## B. Quark-hadron transition model

In our treatment of quark matter, the BHF framework is adopted on the basis of two-body  $QQ$  potentials [36]. Here, correlations induced by bare  $QQ$  potentials are renormalized into coordinate-space  $G$ -matrix interactions, which are considered as effective  $QQ$  interactions used in quark-matter calculations.

Our bare  $QQ$  interaction is given by

$$V_{QQ} = V_{\text{EME}} + V_{\text{INS}} + V_{\text{OGE}} + V_{\text{MPP}} \quad (2.9)$$

where  $V_{\text{EME}}$ ,  $V_{\text{INS}}$ ,  $V_{\text{OGE}}$ , and  $V_{\text{MPP}}$  are the extended meson exchange potential, the instanton exchange potential, the one-gluon exchange potential and the multi-Pomeron exchange potential, respectively. Parameters in our  $QQ$  potential are chosen so as to be consistent with physical observables. The  $V_{\text{EME}}$   $QQ$  potential is derived from the ESC  $BB$  potential so that the  $QQM$  couplings are related to the  $BBM$  couplings through folding procedures with Gaussian baryonic quark wave functions. In the construction of the relation between  $BBM$  and  $QQM$  couplings, the requirement that the coefficients of the  $1/M^2$  expansion should match is based on Lorentz invariance, which fixes the  $QQM$  couplings and also determines the (few) extra vertices at the quark level [38]. Then, the  $V_{\text{EME}}$   $QQ$  potential has basically the same functional expression as the ESC  $BB$  potential. Strongly repulsive components in ESC  $BB$  potentials are described mainly by vector-meson and pomeron exchanges between baryons. This feature persists in the  $V_{\text{EME}}$   $QQ$  potential, which includes the strongly repulsive components originating from vector-meson and Pomeron exchanges between quarks. Similarly the multi-Pomeron exchange potentials among quarks,  $V_{\text{MPP}}$ , are derived from the corresponding ones among baryons, giving repulsive contributions. Contributions from  $V_{\text{INS}}$  and  $V_{\text{OGE}}$  on average are attractive and repulsive, respectively. The strength of  $V_{\text{OGE}}$  is determined by the quark-gluon coupling constant  $\alpha_s$ . In [36]  $\alpha_s$  is chosen as 0.25, that is  $V_{\text{OGE}}(\alpha_s = 0.25)$ , and the three sets are defined as Q0:  $V_{\text{EME}}$ ; Q1:  $V_{\text{EME}} + V_{\text{INS}} + V_{\text{OGE}}(\alpha_s = 0.25)$ ; Q2:  $V_{\text{EME}} + V_{\text{MPP}} + V_{\text{INS}} + V_{\text{OGE}}(\alpha_s = 0.25)$ .

In our QHT model for neutron-star matter, quark-hadron phase transitions occur at crossing points of hadron pressure

$P_H(\mu)$  and quark pressure, which are functions of chemical potential  $\mu$ . Positions of crossing points, giving quark-hadron transition densities, are controlled by parameters  $\rho_c$  and  $\gamma$  included in our density-dependent quark mass

$$M_Q^*(\rho_Q) = \frac{M_0}{1 + \exp[\gamma(\rho_Q - \rho_c)]} + m_0 + C, \quad (2.10)$$

with  $C = M_0 - M_0/[1 + \exp(-\gamma\rho_c)]$  assuring  $M_Q^*(0) = M_0 + m_0$ , where  $\rho_Q$  is number density of quark matter, and  $M_0$  and  $m_0$  are taken as 300 (360) MeV and 5 (140) MeV for  $u$  and  $d$  ( $s$ ) quarks. Here, the effective quark mass  $M_Q^*(\rho_Q)$  should be used together with  $B(\rho_Q) = M_Q^*(0) - M_Q^*(\rho_Q) + B_0$ , meaning the energy-density difference between the perturbative vacuum and the true vacuum. A constant term  $B_0$  is added for fine tuning of an onset density. In [36], the values of  $(\rho_c, \gamma)$  without  $B_0$  are given for each set of Q0, Q1, and Q2.

Let us focus on the typical result for Q2 + H1 in [36]. The  $QQ$  interaction Q2 is the most repulsive among Q0, Q1, and Q2. The  $BB$  interaction H1 consists of ESC and MPb, and results in the reasonable value of  $R_{1.4M_\odot}$ . In this case of Q2+H1, we obtain the maximum mass of  $2.25M_\odot$  and the reasonable value of  $R_{1.4M_\odot} = 12.5$  km, in which the quark-hadron transition occurs at a density of  $3.5\rho_0$ . Then, we have  $R_{2.0M_\odot} = 12.0$  km, which is rather smaller than 12.4 km in the criterion (1.1). In order to reproduce a larger value of  $R_{2.0M_\odot} \approx 12.4$  km, we make  $V_{\text{OGE}}$  more repulsive by taking larger values of  $\alpha_S = 0.36$  and  $0.49$ . It is not suitable for such a purpose to strengthen the  $V_{\text{MPP}}$  repulsion, because  $V_{\text{MPP}}$  is essentially of three-body interaction and the contributions in the low-density region are small. On the other hand,  $V_{\text{OGE}}$  is of two-body interaction, and its repulsive contributions are not small even in low density region, which is important for a large value of  $R_{2.0M_\odot}$ . Another condition to make  $R_{2.0M_\odot}$  larger is to lower quark-hadron transition densities by adjusting the parameters  $(\rho_c, \gamma, B_0)$  included in the density-dependent quark mass, Eq. (2.10).

We define the following three sets with the fixed value of  $\gamma = 1.2$ :

$$\begin{aligned} \text{Q2: } & V_{\text{EME}} + V_{\text{MPP}} + V_{\text{INS}} + V_{\text{OGE}}(\alpha_S = 0.25) \\ & \text{with } \rho_c = 6.9\rho_0 \text{ and } B_0 = 8.5, \\ \text{Q3: } & V_{\text{EME}} + V_{\text{MPP}} + V_{\text{INS}} + V_{\text{OGE}}(\alpha_S = 0.36) \\ & \text{with } \rho_c = 6.9\rho_0 \text{ and } B_0 = 7.5, \\ \text{Q4: } & V_{\text{EME}} + V_{\text{MPP}} + V_{\text{INS}} + V_{\text{OGE}}(\alpha_S = 0.69) \\ & \text{with } \rho_c = 7.5\rho_0 \text{ and } B_0 = 10.0, \end{aligned}$$

where the values of  $\rho_c$  and  $B_0$  for each set are chosen so as to give quark-hadron transition densities of  $\sim 2\rho_0$ .

$G$ -matrix interactions  $\mathcal{G}_{qq'}$  with  $q, q' = u, d, s$  are derived from the above bare  $QQ$  interactions. They are given for each  $(qq', T, S, P)$  state,  $T, S,$  and  $P$  being isospin, spin and parity in a two-body state, respectively, and represented as  $\mathcal{G}_{qq'}^{TSP}$ . Hereafter, Q2, Q3, and Q4 represent corresponding  $QQ$   $G$ -matrix interactions, not only bare  $QQ$  interactions. The  $QQ$   $G$ -matrix interactions are used also in the quarkyonic matter calculations.

A single quark potential is given by

$$U_q(k) = \sum_{q'=u,d,s} U_q^{(q')}(k) = \sum_{q'=u,d,s} \sum_{k' < k_F^{q'}} \langle kk' | \mathcal{G}_{qq'} | kk' \rangle \quad (2.11)$$

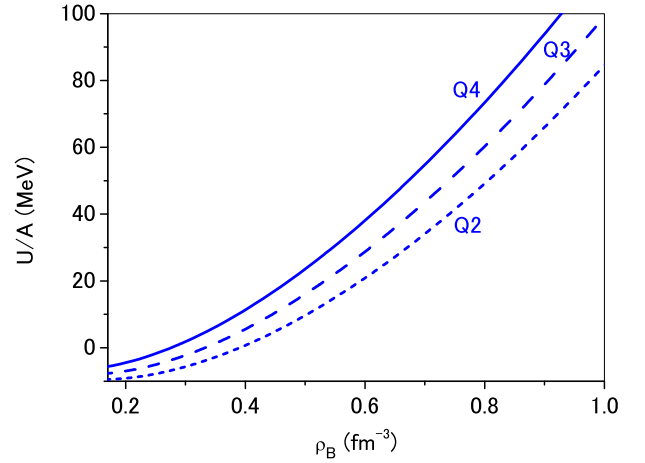


FIG. 1. Potential energies per particle  $U/A$  as a function of the baryon number density  $\rho_B$  in the case of  $\rho_u = \rho_d = \rho_s$ . The short-dashed, long-dashed, and solid curves are obtained by using Q2, Q3, and Q4, respectively.

with  $q = u, d, s$ , where  $k_F^q$  is the Fermi momentum of quark  $q$ . Spin and isospin quantum numbers are implicit.

The quark energy density is given by

$$\begin{aligned} \varepsilon_q &= g_s N_c \sum_{q=u,d,s} \int_0^{k_{Fq}} \frac{d^3k}{(2\pi)^3} \\ &\times \left\{ \sqrt{\hbar^2 k^2 + M_q^2} + \frac{1}{2} U_q(k) \right\}. \quad (2.12) \end{aligned}$$

Fermion spin and quark color degeneracies give rise to  $g_s = 2$  and  $N_c = 3$ .

In order to demonstrate the features of our  $QQ$  interactions (Q2, Q3, Q4), we show the potential energy per particle  $U/A$  as a function of the baryon number density  $\rho_B = \frac{1}{3}\rho_Q$  in the case of taking  $\rho_u = \rho_d = \rho_s$ . In Fig. 1, the short-dashed, long-dashed, and solid curves are obtained by using Q2, Q3, and Q4, respectively. The repulsions are found to be strong in the order of Q4, Q3, Q2. This difference of repulsions among Q4, Q3, and Q2 comes from the different values of  $\alpha_S$  included in  $V_{\text{OGE}}$ . In the figure, it should be noted that the difference is not small even in the low-density region.

In the EoS of  $\beta$ -stable quark matter composed of  $u, d, s, e^-$ , the equilibrium conditions are given as

(1) chemical equilibrium conditions,

$$\mu_d = \mu_s = \mu_u + \mu_e, \quad (2.13)$$

(2) charge neutrality,

$$0 = \frac{1}{3}(2\rho_u - \rho_d - \rho_s) - \rho_e, \quad (2.14)$$

(3) baryon number conservation,

$$\rho_B = \frac{1}{3}(\rho_u + \rho_d + \rho_s) = \frac{1}{3}\rho_Q. \quad (2.15)$$

In order to construct the hybrid EoS including a transition from hadronic phase to quark phase, we use the replacement interpolation method [33,36], which is a simple modification of the Maxwell and the Glendenning (Gibbs) constructions [51]. The EoSs of hadronic and quark phases and that of mixed



phase are described with the relations between pressures and chemical potentials  $P_H(\mu)$ ,  $P_Q(\mu)$ , and  $P_M(\mu)$ , respectively. The critical chemical potential  $\mu_c$  for the transition from the hadronic phase to the quark phase is obtained from the Maxwell condition

$$P_Q(\mu_c) = P_H(\mu_c) = P_c. \quad (2.16)$$

The pressure of the mixed phase is represented by a polynomial ansatz. The matching densities  $\rho_H$  and  $\rho_Q$  are obtained with use of  $\rho(\mu) = dP(\mu)/d\mu$ .

### C. Quarkyonic matter

In the BHF framework, we derive the EoS of quarkyonic matter composed of neutrons and quarks with flavor  $q = u, d$  in the simplest form by McLerran and Reddy [43]. In chargeless two-flavor quarkyonic matter, strongly interacting quarks near the Fermi sea form interacting neutrons, and the remaining  $d$  and  $u$  quarks fill the lowest momenta up to  $k_{Fu}$  and  $k_{Fd}$ , respectively. The quark mass is taken to be  $M_q = M_n/3$  constantly,  $M_n$  being the neutron mass. In calculations of quarkyonic matter, we use B1 ( $V_{nn}$ ) and B2 ( $V_{nn} + V_{nnn}$ ) for nuclear interactions, and Q0 for  $QQ$  interactions for simplicity.

The total baryon number density is given by

$$\begin{aligned} \rho_B &= \rho_n + \frac{N_c}{3}(\rho_u + \rho_d) \\ &= \frac{g_s}{6\pi^2} \left[ k_{Fn}^3 - k_{0n}^3 + \frac{N_c}{3}(k_{Fu}^3 + k_{Fd}^3) \right], \end{aligned} \quad (2.17)$$

where  $k_{Fn}$ ,  $k_{Fu}$ , and  $k_{Fd}$  are the Fermi momenta of neutrons and  $u$  and  $d$  quarks, respectively. Fermion spin and quark color degeneracies give rise to  $g_s = 2$  and  $N_c = 3$ . Neutrons are restricted near the Fermi surface by  $k_{0n}$ , assumed to be

$$\begin{aligned} k_{0n} &= k_{Fn} - \Delta_{qyc}, \\ \Delta_{qyc} &= \frac{\Lambda^3}{\hbar c^3 k_{Fn}^2} + \kappa \frac{\Lambda}{N_c^2 \hbar c}, \end{aligned} \quad (2.18)$$

where  $\Delta_{qyc}$  for the thickness of Fermi layer includes the two parameters  $\Lambda$  and  $\kappa$ . In this work, we take the fixed value of  $\kappa = 0.3$ .

Then,  $k_{Fd}$  and  $k_{Fu}$  are related to  $k_{0n}$  by  $k_{Fd} = \frac{1}{N_c} k_{0n}$  and  $k_{Fu} = 2^{-1/3} k_{Fd}$ .

A single neutron potential is given by

$$U_n(k) = \sum_{k_{0n} < k' < k_{Fn}} \langle kk' | \mathcal{G}_{nn} | kk' \rangle \quad (2.19)$$

with  $nn$   $G$ -matrix interactions  $\mathcal{G}_{nn}$ .

The neutron energy density is given by

$$\begin{aligned} \varepsilon_n &= \tau_n + \nu_n \\ &= g_s \int_{k_{0n}}^{k_{Fn}} \frac{d^3k}{(2\pi)^3} \left\{ \sqrt{\hbar^2 k^2 + M_n^2} + \frac{1}{2} U_n(k) \right\}. \end{aligned} \quad (2.20)$$

Additionally, another form of the neutron potential energy density is defined as

$$\bar{\nu}_n = g_s \int_0^{k_n} \frac{d^3k}{(2\pi)^3} \left\{ \frac{1}{2} U_n(k) \right\}, \quad (2.21)$$

which is used in [43] instead of  $\nu_n$ .

Single quark potentials for  $q = u, d$  are given by

$$\begin{aligned} U_q(k) &= \sum_{q'=u,d} U_q^{(q')}(k) \\ &= \sum_{q'=u,d} \sum_{k' < k_{Fq}} \langle kk' | \mathcal{G}_{qq'} | kk' \rangle, \end{aligned} \quad (2.22)$$

$$U_q^{(n)}(k) = \sum_{k_{0n} < k' < k_{Fn}} \langle kk' | \mathcal{G}_{qn} | kk' \rangle, \quad (2.23)$$

with  $G$ -matrix interactions  $\mathcal{G}_{qq'}$  and  $\mathcal{G}_{qn}$ . Here,  $\mathcal{G}_{qn}$  is the quark-neutron ( $Qn$ ) interaction: We assume the simple model in which the potentials  $\mathcal{G}_{qq'}$  are folded into the potentials  $\mathcal{G}_{qn}$  with Gaussian baryonic quark wave functions. In Eqs. (2.19), (2.22), and (2.23) spin quantum numbers are implicit.

The quark energy density is given by

$$\begin{aligned} \varepsilon_q &= g_s N_c \sum_{q=u,d} \int_0^{k_{Fq}} \frac{d^3k}{(2\pi)^3} \\ &\times \left\{ \sqrt{\hbar^2 k^2 + M_q^2} + \frac{1}{2} U_q(k) + U_{qn}(k) \right\}, \end{aligned} \quad (2.24)$$

where values of  $k_{Fq}$  are determined by

$$N_c k_{Fq} = k_{0n}. \quad (2.25)$$

Thus, our total energy density is given by

$$\varepsilon = \varepsilon_n + \varepsilon_d + \varepsilon_u. \quad (2.26)$$

The chemical potential  $\mu_i$  ( $i = n, d, u$ ) and pressure  $P$  are expressed as

$$\mu_i = \frac{\partial \varepsilon_i}{\partial n_i}, \quad (2.27)$$

$$P = \sum_{i=n,d,u} \mu_i n_i - \varepsilon, \quad (2.28)$$

where  $\frac{\partial \varepsilon_i}{\partial n_i} = \frac{\partial \varepsilon_i}{\partial n_B} \frac{\partial n_B}{\partial n_i}$ .

In our model, the phase transition from  $\beta$ -stable nucleonic matter to the quarkyonic matter occurs in second order, resulting in a hybrid EoS including hadronic and quarkyonic EoSs. Then, the transition densities are controlled mainly by the parameter  $\Lambda$ : In this work, we choose the three values of  $\Lambda = 380, 350, \text{ and } 320$  MeV with the fixed value of  $\kappa = 0.3$ . The transition densities for these values are  $0.28\text{--}0.38$  fm $^{-3}$  ( $0.28\text{--}0.36$  fm $^{-3}$ ) in the case of using B1 (B2) for nuclear interactions. Hereafter, when a value of  $\Lambda = 380$  MeV is used, for instance, it is denoted as  $\Lambda 380$ .

## III. RESULTS AND DISCUSSION

### A. EoS

In Fig. 2, pressures  $P$  are drawn as a function of baryonic number density  $\rho_B$ . The dot-dashed curve is for the  $\beta$ -stable nucleonic-matter EoS, and the dotted one is for the  $\beta$ -stable hadronic-matter EoS with hyperon mixing. The latter is substantially below the former, demonstrating the EoS softening by hyperon mixing. Thin (thick) solid curves in the upper side are pressures in the quarkyonic matter for  $\Lambda 350$  and  $\Lambda 320$

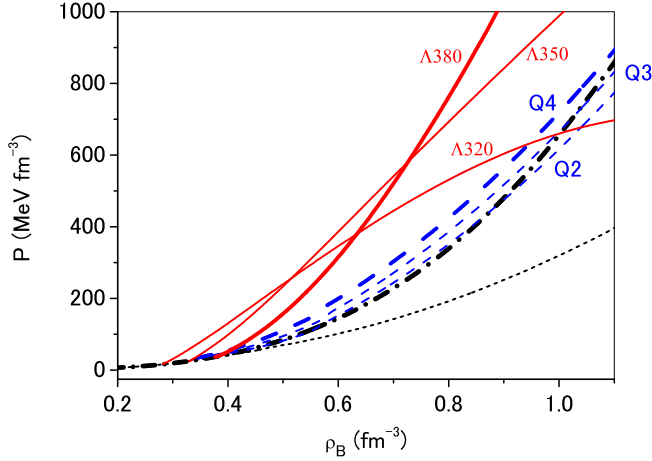


FIG. 2. Pressures  $P$  as a function of baryonic number density  $\rho_B$ . The dot-dashed (dotted) curve is for  $\beta$ -stable nucleonic (hadronic) matter. Upper thin (thick) solid curves are pressures in the quarkyonic matter for  $\Lambda 350$  and  $\Lambda 320$  ( $\Lambda 380$ ) with B1. Lower thin (thick) short-dashed curves are for the QHT matter with Q2 and Q3 (Q4).

( $\Lambda 380$ ) with use of B1 for nuclear interactions. At the crossing points with the dot-dashed curve in the low-density side, there occur second-order transitions from  $\beta$ -stable nucleonic to quarkyonic phases: The transition densities  $\rho_t$  are 0.38, 0.33, 0.28  $\text{fm}^{-3}$  ( $2.2\rho_0$ ,  $1.9\rho_0$ ,  $1.6\rho_0$ ) in the cases of  $\Lambda 380$ ,  $\Lambda 350$ , and  $\Lambda 320$ , respectively. Thin (thick) short-dashed curves are for the QHT models with Q2 and Q3 (Q4). It should be noted that pressures in the quarkyonic matter increase more rapidly with density than those in the QHT matter. As discussed later, the rapid growth of pressure with density in the range of  $2\rho_0$ – $4\rho_0$  is an important feature of the quarkyonic model. This rapid increase of pressure at onset of the quarkyonic phase influences significantly the neutron-star  $MR$  curves.

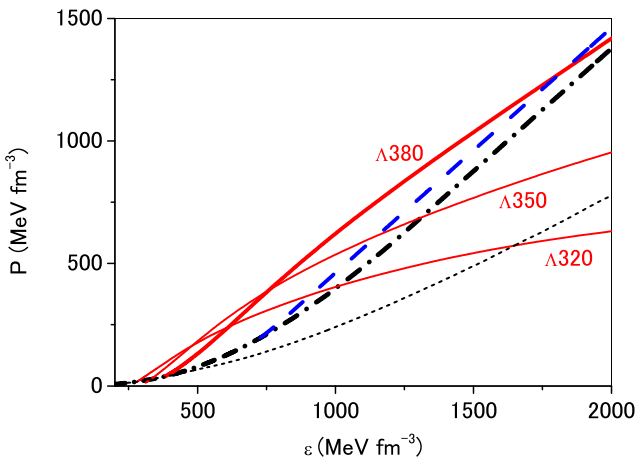


FIG. 3. Pressures  $P$  as a function of the energy density  $\varepsilon$ . The dot-dashed (dotted) curves are for  $\beta$ -stable nucleonic (hadronic) matter. Thin (thick) solid curves show pressures in quarkyonic phases for  $\Lambda 350$  and  $\Lambda 320$  ( $\Lambda 380$ ) with B1. The short-dashed curve is for the QHT model with Q4.

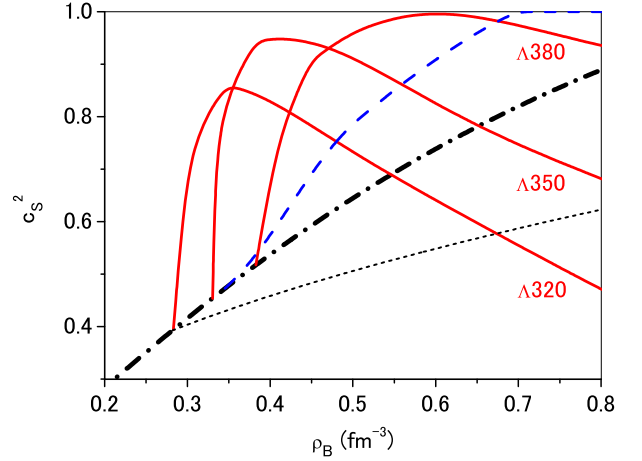


FIG. 4. The square of the sound speed,  $c_s^2$ , in units of  $c^2$  as a function of baryonic number density  $\rho_B$ . The dot-dashed (dotted) curve is that in  $\beta$ -stable nucleonic (hadronic) matter. Solid curves are pressures in quarkyonic matter for  $\Lambda 380$ ,  $\Lambda 350$  and  $\Lambda 320$  with B1. The dashed curve is for the QHT matter with Q4.

In Fig. 3, pressures  $P$  are drawn as a function of the energy density  $\varepsilon$ , which are related closely to neutron-star  $MR$  curves. The dot-dashed (dotted) curve shows pressures in  $\beta$ -stable nucleonic (hadronic) matter. Thin (thick) solid curves show pressures in quarkyonic matter for  $\Lambda 350$  and  $\Lambda 320$  ( $\Lambda 380$ ) with B1. The short-dashed curve is for the QHT matter with Q4. Though the curves for Q4 and  $\Lambda 380$  are rather similar to each other in comparison with the corresponding curves in Fig. 2, the former is still less steep than the latter in the region of low energy density. As shown later, the EoSs for the QHT model Q4 and the quarkyonic model  $\Lambda 380$  lead to neutron-star  $MR$  curves consistent with the criterion (1.1).

In Fig. 4, sound velocities are drawn as a function of  $\rho_B$ . The dot-dashed curve is sound velocity in  $\beta$ -stable nucleonic matter. Solid curves are those in quarkyonic matter for  $\Lambda 380$ ,  $\Lambda 350$ , and  $\Lambda 320$  with B1. There appear peak structures in the solid curves, which are related to rapid increase of pressures in the range  $2\rho_0$ – $4\rho_0$ . The dashed curve is sound velocity in the QHT matter with Q4 and the dotted one is that in  $\beta$ -stable hadronic matter with hyperon mixing, in which there appears no peak structure. The dashed curve becomes  $c_s > c$  in the high-density region. Also, the peak regions of solid curves become  $c_s > c$ , if B2 is used instead of B1 for nuclear parts. In such regions of  $c_s > c$ , sound velocities are approximated to be  $c_s = c$ .

It is interesting to notice that the peak structures in our quarkyonic-matter results are somewhat similar to those for the QHC-matter EoS (QHC21) found in [35]. Our QHT-matter EoS gives no peak structure in sound velocities, which is different from both of them.

In the left panel of Fig. 5, solid curves show pressures in quarkyonic matter for  $\Lambda 380$  in the cases of using B1 and B2 for nuclear interactions, and short-dashed (dashed) curves are partial pressures of neutrons (quarks) in respective cases. The dot-dashed curve is pressure in  $\beta$ -stable nucleonic matter. Pressures in quarkyonic matter are found to be completely

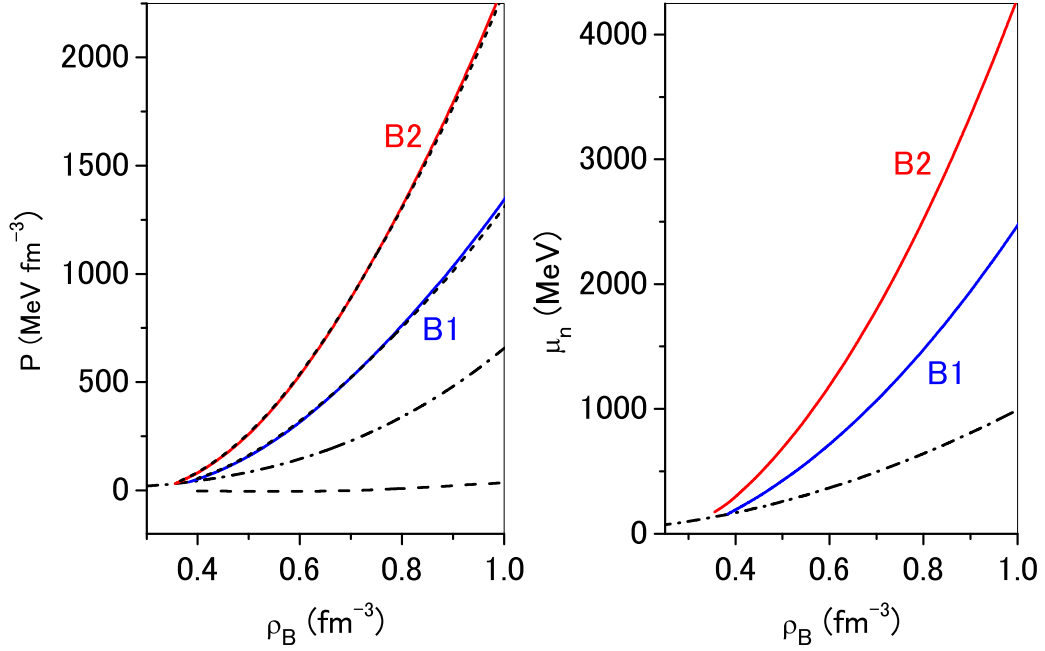


FIG. 5. In the left panel, solid curves are pressures  $P$  in quarkyonic phases as a function of baryonic number density  $\rho_B$  for  $\Lambda 380$  in the cases of using B1 and B2, and short-dashed (dashed) curves are partial pressures of neutrons (quarks) in respective cases. The dot-dashed curve is for  $\beta$ -stable nucleonic matter. In the right panel, solid (dot-dashed) curves are neutron chemical potentials  $\mu_n$  in quarkyonic ( $\beta$ -stable nucleonic) phases as a function of  $\rho_B$  for  $\Lambda 380$  in the cases of using B1 and B2. The dot-dashed curve gives the neutron chemical potential in  $\beta$ -stable nucleonic matter.

dominated by neutron partial pressures. In order to reveal the reason why neutron pressures in quarkyonic matter are far higher than those in  $\beta$ -stable nucleonic matter, we show the neutron chemical potentials in the cases of using B1 and B2 for nuclear interactions: In the right panel of Fig. 5, neutron chemical potentials  $\mu_n$  are drawn as a function of  $\rho_B$ . Lower and upper solid curves give neutron chemical potentials in quarkyonic matter for  $\Lambda 380$  in the cases of using B1 and B2, respectively. The dot-dashed curve gives the neutron chemical potential in  $\beta$ -stable nucleonic matter. The neutron chemical potentials in quarkyonic matter are far higher than those in the  $\beta$ -stable nucleonic matter, which makes neutron pressures in the former far higher than those in the latter. The reason for higher chemical potentials in the quarkyonic matter is because the existence of free quarks inside the Fermi sea gives nucleons extra kinetic energies by pushing them to higher momenta [43].

### B. MR diagrams

We have the two types of hybrid EoSs: the QHT-matter EoS and the quarkyonic-matter EoS. They are combined with the  $\beta$ -stable nucleonic-matter EoS and connected smoothly to the crust EoS [52,53] on the low-density side. The  $MR$  relations of hybrid stars can be obtained by solving the TOV equations with these hybrid EoSs.

In Fig. 6, star masses are given as a function of radius  $R$ . The dot-dashed curves are obtained by the  $\beta$ -stable nucleonic matter EoS. In the left panel, thin (thick) solid curves are obtained by the QHT-matter EoSs with Q2 and Q3 (Q4).

The dotted curve is by the hadronic-matter EoS including hyperons. In the cases of Q2, Q3, and Q4, the maximum masses are  $M_{\max}/M_{\odot} = 2.23, 2.30, 2.40$ , respectively, and the radii at  $2.0M_{\odot}$  are 11.8, 12.2, 12.5 km, respectively. In the right panel, thin (thick) solid curves are obtained by the quarkyonic-matter EoSs for  $\Lambda 350$  and  $\Lambda 320$  ( $\Lambda 380$ ) using B1 for nuclear interactions. In the cases of  $\Lambda 380$ ,  $\Lambda 350$ , and  $\Lambda 320$ , the maximum masses are  $M_{\max}/M_{\odot} = 2.64, 2.79, 2.76$ , respectively, and the radii at  $2.0M_{\odot}$  are 12.6, 13.1, 13.5 km, respectively. In both panels, the horizontal lines indicate  $R_{1.4M_{\odot}} = 12.56^{+1.00}_{-1.07}$  km and  $R_{2.0M_{\odot}} = 12.41^{+1.00}_{-1.10}$  km, and the rectangle indicates the region of mass  $M_{\max}/M_{\odot} = 2.21^{+0.31}_{-0.21}$  [7]. The thick solid curve for Q4 in the left panel and that for  $\Lambda 380$  in the right panel are found to be consistent with the criterion (1.1), and the key features of  $R_{2M_{\odot}} \approx R_{1.4M_{\odot}}$  are found in these cases.

Then, it should be noted that the maximum mass  $2.64M_{\odot}$  for  $\Lambda 380$  is substantially larger than the value  $2.40M_{\odot}$  for Q4. The reason for such a difference between maximum masses can be understood by comparing the  $P(\rho_B)$  curves in Fig. 2, where the solid curve for  $\Lambda 380$  increases more rapidly at the onset of quarkyonic matter than the dashed curve for Q4 at the onset of quark matter. This means that the stiffness for the former is larger than that for the latter. In the case of QHT matter, it is not possible to obtain such a rapid increase of  $P(\rho_B)$  in the low-density region, even if the  $QQ$  repulsions are strengthened.

In the case of hadronic (nucleonic) matter, shown by the dotted (dot-dashed) curve in the left panel, the maximum mass is  $1.82M_{\odot}$  ( $2.19M_{\odot}$ ). The reduction of  $0.37M_{\odot}$  is due

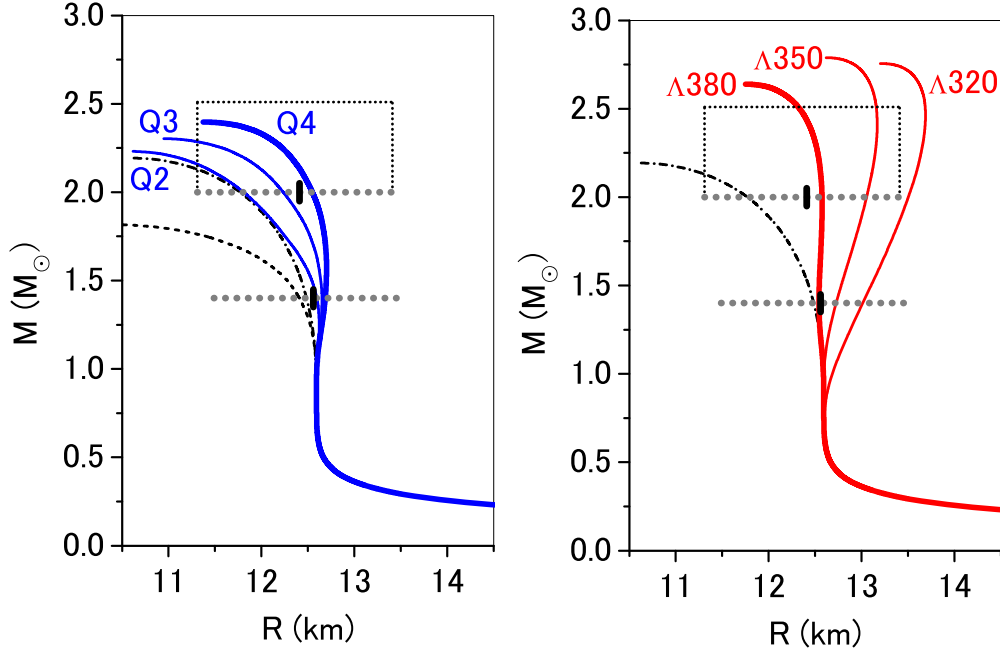


FIG. 6. Star masses as a function of radius  $R$ . The dot-dashed curves are from using the  $\beta$ -stable nucleonic matter EoS. In the left panel, thin (thick) solid curves are from the QHT-matter EoSs with Q2 and Q3 (Q4). The dotted curve is from the hadronic matter EoS including hyperons. In the right panel, thin (thick) solid curves are by the quarkyonic-matter EoSs for  $\Lambda 350$  and  $\Lambda 320$  ( $\Lambda 380$ ) with B1. In both panels, the horizontal lines indicates  $R_{1.4M_\odot} = 12.56^{+1.00}_{-1.07}$  km and  $R_{2.0M_\odot} = 12.41^{+1.00}_{-1.10}$  km, and the rectangle indicates the region of mass  $M_{\max}/M_\odot = 2.21^{+0.31}_{-0.21}$  [7].

to the EoS softening by hyperon ( $\Lambda$  and  $\Sigma^-$ ) mixing. This softening is mainly caused by  $\Sigma^-$  mixing: If only  $\Lambda$  mixing is taken into account, the maximum mass is obtained as  $2.06M_\odot$ , which is close to the value of  $2.19M_\odot$  without hyperon mixing (dot-dashed curve). Thus, massive stars with  $M > 2M_\odot$  cannot be obtained by the hadronic matter EoSs with hyperon ( $\Lambda$  and  $\Sigma^-$ ) mixing [14–16]. On the other hand, the value of  $R_{1.4M_\odot}$  is 12.4 (12.5) km in the case of hadronic (nucleonic) matter, which means that the hyperon mixing does not depend much on  $R_{1.4M_\odot}$ .

In Fig. 7, star masses are given as a function of central baryon density  $\rho_{Bc}$ . The dot-dashed curves are by the  $\beta$ -stable nucleonic matter EoS. The solid curve is obtained by the quarkyonic-matter EoS for  $\Lambda 380$  with B1, and the dashed curve is by the QHT-matter EoS for Q4, where the onset density in the former (latter)  $0.39$  ( $0.33$ )  $\text{fm}^{-3}$ . Both of them are consistent with Eq. (1.1), but the former mass curve for  $\rho_{Bc}$  is considerably above the latter one, as well as the corresponding  $MR$  curves.

In Fig. 8, star masses are given as a function of radius  $R$ . The solid curve is obtained by the quarkyonic-matter EoS for  $\Lambda 380$  with use of B1 ( $V_{nn}$ ) for nuclear interactions, given also in Fig. 6. Dashed and short-dashed curves are by the quarkyonic-matter EoSs for  $\Lambda 380$  and  $\Lambda 400$ , respectively, in the case of using B2 ( $V_{nn} + V_{nnn}$ ) instead of B1. The difference between solid and dashed curves demonstrates the effect of the three-neutron repulsion  $V_{nnn}$ , giving the larger maximum mass and larger value of  $R_{2.0M_\odot}$ . The short-dashed curve for  $\Lambda 400$  indicates that this effect of  $V_{nnn}$  to increase mass and radius is canceled out by taking larger values of  $\Lambda$ .

In Fig. 9, star masses are given as a function of radius  $R$ . The solid curve is obtained by the quarkyonic-matter EoS for  $\Lambda 380$  with  $\kappa = 0.3$  in the case of using B1, given also in Fig. 6. The dashed curve is obtained by the approximation used in [43], where the  $QQ$  interactions are neglected and the quark energy density Eq. (2.24) is replaced by the kinetic energy density. Then, the difference between short-dashed and dashed curves is due to this approximation. The short-dashed

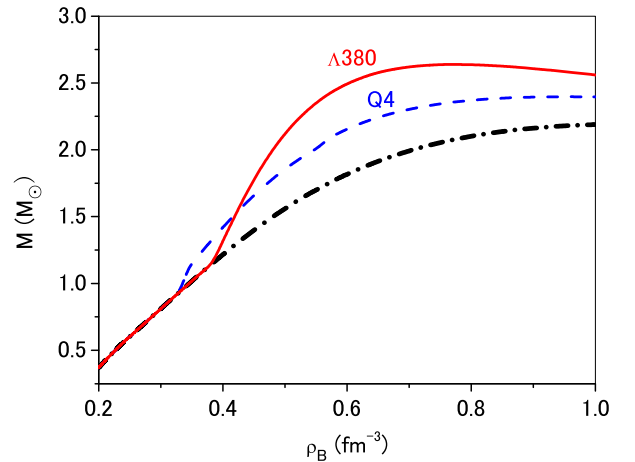


FIG. 7. Star masses as a function of central baryon density  $\rho_{Bc}$ . The dot-dashed curves are from using the  $\beta$ -stable nucleonic EoS. The solid curve is from the quarkyonic-matter EoS for  $\Lambda 380$  in the case of using B1. The short-dashed curve is from the QHT-matter EoS for Q4.



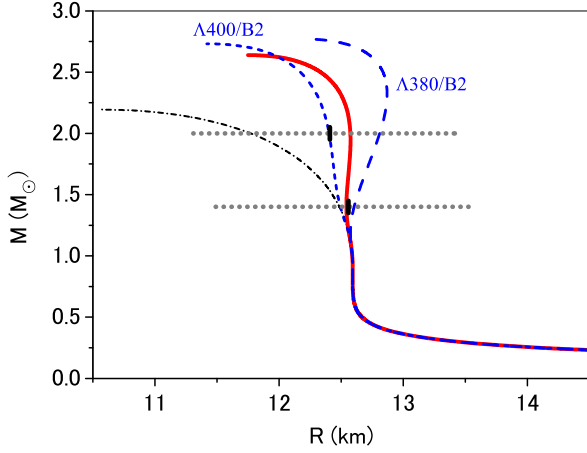


FIG. 8. Star masses as a function of radius  $R$ . The dot-dashed curves are from using the  $\beta$ -stable nucleonic matter EoS. The solid curve is for  $\Lambda 380$  with B1. Dashed and short-dashed curves are from the quarkyonic-matter EoSs for  $\Lambda 380$  and  $\Lambda 400$  with B2, respectively. The horizontal dotted lines indicate  $R_{1.4M_\odot} = 12.56^{+1.00}_{-1.07}$  km and  $R_{2.0M_\odot} = 12.41^{+1.00}_{-1.10}$  km.

curve is obtained by taking  $\kappa = 0.4$  under this approximation. The similarity between solid and short-dashed curves means that the deviation due to this approximation is canceled out by adjusting the value of  $\kappa$ . In the same case of  $\Lambda 380$  and  $\kappa = 0.3$  with B1, the dotted curve is obtained by replacing the potential energy density in Eq. (2.20) with Eq. (2.21), which is the approximated treatment in [43]. This approximation using Eq. (2.21) is found to reduce masses and to increase radii.

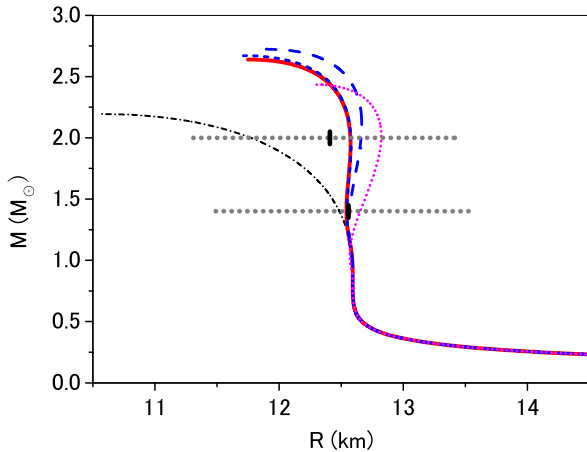


FIG. 9. Star masses as a function of radius  $R$ . The dot-dashed curves are from using the  $\beta$ -stable nucleonic matter EoS. The solid curve is obtained by the quarkyonic-matter EoS for  $\Lambda 380$  with  $\kappa = 0.3$  in the case of using B1. The dashed (short-dashed) curve is for  $\Lambda 380$  with  $\kappa = 0.3$  ( $\kappa = 0.4$ ) using the approximation to neglect potential sectors in quark energy densities. The dotted curve is obtained by replacing the potential energy density in Eq. (2.20) with Eq. (2.21). The horizontal lines indicate  $R_{1.4M_\odot} = 12.56^{+1.00}_{-1.07}$  km and  $R_{2.0M_\odot} = 12.41^{+1.00}_{-1.10}$  km.

TABLE I. Maximum masses  $M_{\max}$ , pressures  $p$  at  $\rho_0$ ,  $2\rho_0$ , and  $6\rho_0$ , radii  $R$  and tidal deformabilities  $\Lambda$  at  $1.4M_\odot$  and  $2.0M_\odot$ , and central densities  $\rho_c$  at  $1.4M_\odot$ ,  $2.0M_\odot$ , and  $M_{\max}$ . Results for the  $\beta$ -stable nucleonic matter EoS denoted as NUC, the QHT-matter EoS Q4, and the quarkyonic matter EoS  $\Lambda 380$  are compared with the values taken from [7].

	NUC	Q4	$\Lambda 380$	Ref. [7]
$M_{\max}/M_\odot$	2.19	2.40	2.64	$2.21^{+0.31}_{-0.21}$
$p(\rho_0)$ ( $10^{33}$ dyn/cm $^2$ )	5.27	5.27	5.27	$4.30^{+3.37}_{-3.80}$
$p(2\rho_0)$ ( $10^{34}$ dyn/cm $^2$ )	2.76	5.09	4.42	$4.38^{+2.46}_{-2.96}$
$p(6\rho_0)$ ( $10^{35}$ dyn/cm $^2$ )	6.94	12.0	22.6	$7.41^{+5.87}_{-4.18}$
$R_{1.4M_\odot}$ (km)	12.5	12.7	12.5	$12.56^{+1.00}_{-1.07}$
$R_{2.0M_\odot}$ (km)	11.8	12.5	12.6	$12.41^{+1.00}_{-1.10}$
$R_{2.0M_\odot} - R_{1.4M_\odot}$ (km)	-0.72	-0.14	+0.03	$-0.12^{+0.83}_{-0.85}$
$\Lambda_{1.4}$	779	525	473	$507^{+234}_{-242}$
$\Lambda_{2.0}$	128	46	49	$44^{+34}_{-30}$
$\rho_c(1.4M_\odot)$ ( $10^{14}$ g/cm $^3$ )	7.9	6.6	6.8	$6.7^{+1.7}_{-1.3}$
$\rho_c(2.0M_\odot)$ ( $10^{14}$ g/cm $^3$ )	12.	9.1	8.0	$9.7^{+3.6}_{-3.1}$
$\rho_c(M_{\max})$ ( $10^{15}$ g/cm $^3$ )	1.8	1.6	1.3	$1.5^{+0.3}_{-0.4}$

### C. Discussion

In [7], the authors present neutron-star properties such as maximum mass, radius, tidal deformability, pressure, and central density inferred from their analysis, for which the median and 90% highest-probability-density credible regions are given. From Table II of [7], we choose the quantities in the case labeled w/J0740 + 6620 Miller + in order to compare with the corresponding values obtained from our QHT-matter and the quarkyonic matter EoSs. In Table I we tabulated maximum masses  $M_{\max}$ , pressures  $p$  at  $\rho_0$ ,  $2\rho_0$ , and  $6\rho_0$ , radii  $R$  and dimensionless tidal deformabilities  $\Lambda$  at  $1.4M_\odot$  and  $2.0M_\odot$ , and central densities  $\rho_c$  at  $1.4M_\odot$ ,  $2.0M_\odot$ , and  $M_{\max}$ . Here, our results are for the  $\beta$ -stable nucleonic matter EoS denoted as NUC, the QHT-matter EoS Q4, and the quarkyonic matter EoS  $\Lambda 380$ . These EoSs are adjusted so as to reproduce  $R_{1.4M_\odot}$  with an accuracy of a few hundred meters. Then, the key feature of  $R_{2M_\odot} \approx R_{1.4M_\odot}$  is found in the cases of Q4 and  $\Lambda 380$  EoSs, in contrast to the case of the nucleonic EoS giving  $R_{2M_\odot} < R_{1.4M_\odot}$ . The values of  $R_{2.0M_\odot}$ , central densities, and tidal deformabilities for Q4 and  $\Lambda 380$  EoSs are far closer to the median values than those for the nucleonic EoS, demonstrating the clear impacts of quark phases in Q4 and  $\Lambda 380$  EoSs. The deviations from the median values in the latter case are considerably larger than those in the former cases. Especially, the values of  $\Lambda_{1.4}$  and  $\Lambda_{2.0}$  for the nucleonic EoS are noted to be out of 90% credible regions.

In the case of the quarkyonic matter EoS for  $\Lambda 380$ , the values of  $M_{\max}$  and  $p(6\rho_0)$  are found to be far larger than that for the nucleonic EoS. It is interesting that such a large value of  $M_{\max}$  can be obtained straightforwardly from the quarkyonic-matter EoS, considering the implication of the large mass  $(2.35 \pm 0.17)M_\odot$  for PSR J0952-0607 [4]. The reason why a large value of  $M_{\max}$  is obtained in the case of the quarkyonic matter EoS is because the pressure rises rapidly in the region of  $\rho_B \sim 2\rho_0$ , as found in Fig. 2. In the McLerran-Reddy model of the quarkyonic matter, the

resulting EoS is mainly controlled by the one parameter  $\Delta_{qyc}$  for Fermi-layer thickness. Then, it is difficult to reproduce simultaneously  $M_{\max} = 2.2M_{\odot}$  and  $R_{2.0M_{\odot}} = 12.4$  km.

#### IV. CONCLUSION

The observed masses and radii of neutron stars give constraints on the dense matter EoSs and resulting  $MR$  diagrams. In this sense, the observations of massive stars over  $2M_{\odot}$  and the NICER implication of  $R_{2M_{\odot}} \approx R_{1.4M_{\odot}}$  are critically important for restricting neutron-star matter EoSs. In the case of hadronic matter, even if the nucleonic matter EoS is constructed so as to be stiff enough to give the maximum mass over  $2M_{\odot}$ , the hyperon mixing brings about a remarkable softening of the EoS. The EoS-softening by hyperon mixing can be reduced, for instance, by introducing many-body repulsions which work universally for every kind of baryon. However, such a repulsive effect does not cancel out completely the EoS softening by hyperon mixing: In the case of hadronic matter EoS with hyperon mixing, it is difficult to obtain maximum masses over  $2M_{\odot}$ . The most promising approach to solve this ‘‘hyperon puzzle’’ is to assume the existence of quark phases in inner cores of neutron stars, namely hybrid stars having quark matter in their cores.

When quark deconfinement phase transitions from a hadronic-matter EoS to a sufficiently stiff quark-matter EoS are taken into account in the neutron-star interiors, repulsive effects such as  $QQ$  repulsions in quark phases are needed in order to obtain sufficiently stiff EoSs resulting in massive hybrid stars with masses over  $2M_{\odot}$ . In our QHT matter, it is possible to reproduce maximum masses over  $2M_{\odot}$  consistently with the NICER implication, where the  $QQ$  repulsion is taken to be strong enough and the quark-hadron transition

density is adjusted so as to be about  $2\rho_0$  by tuning of the density dependence of effective quark mass.

In the quarkyonic matter, the degrees of freedom inside the Fermi sea are treated as quarks, and nucleons exist at the surface of the Fermi sea. The existence of free quarks inside the Fermi sea gives nucleons extra kinetic energy by pushing them to higher momenta. This mechanism of increasing pressure is completely different from the above mechanism of EoS stiffening by strong  $QQ$  repulsions in the QHT matter. In calculations of  $MR$  diagrams with the quarkyonic-matter EoS, the critical quantity is the thickness  $\Delta_{qyc}$  of the Fermi layer controlled by the parameters  $\Lambda$  and  $\kappa$ . With a reasonable choice of these parameters, the  $MR$  curves of quarkyonic hybrid stars are obtained so as to be consistent with the NICER implication.

As well as  $R_{2.0M_{\odot}}$ , central densities and tidal deformabilities are inferred from the analysis of the NICER data. The QHT-matter and quarkyonic EoSs can be adjusted so as to reproduce these inferred quantities far closer to the median values than those for the nucleonic matter EoS, demonstrating the clear impacts of quark phases in these cases..

Thus, the reasonable  $MR$  curves of neutron stars can be derived from both QHT-matter and quarkyonic-matter EoSs, having completely different mechanisms to stiffen EoSs. However, when both EoSs are adjusted so as to be consistent with the NICER implication, the maximum mass for the quarkyonic-matter EoS is considerably larger than that for the QHT-matter EoS.

#### ACKNOWLEDGMENTS

The authors would like to thank D. Blaschke for valuable comments and fruitful discussions.

- 
- [1] P. B. Demorest, T. Pennucci, S. M. Ransom, M. S. E. Roberts, and J. W. Hessels, *Nature (London)* **467**, 1081 (2010).
  - [2] J. Antoniadis *et al.*, *Science* **340**, 1233232 (2013).
  - [3] H. T. Cromartie *et al.*, *Nat. Astron.* **4**, 72 (2020).
  - [4] R. W. Romani *et al.*, *Astrophys. J. Lett.* **934**, L17 (2022).
  - [5] M. C. Miller *et al.*, *Astrophys. J. Lett.* **918**, L28 (2021).
  - [6] T. E. Riley *et al.*, *Astrophys. J. Lett.* **918**, L27 (2021).
  - [7] I. Legred, K. Chatziioannou, R. Essick, S. Han, and P. Landry, *Phys. Rev. D* **104**, 063003 (2021).
  - [8] I. Bednarek, P. Haensel, J. L. Zdunik, M. Bejger, and R. Mañka, *Astron. Astrophysics, A&A*, **A157**, 543 (2012).
  - [9] S. Weissenborn, D. Chatterjee, and J. Schaffner-Bielich, *Nucl. Phys. A* **881**, 62 (2012).
  - [10] M. Oertel, C. Providência, F. Gulminelli, and A. R. Raduta, *J. Phys. G: Nucl. Part. Phys.* **42**, 075202 (2015).
  - [11] K. A. Maslov, E. E. Kolomeitsev, and D. N. Voskresensky, *Phys. Lett. B* **748**, 369 (2015).
  - [12] S. Nishizaki, Y. Yamamoto, and T. Takatsuka, *Prog. Theor. Phys.* **105**, 607 (2001); **108**, 703 (2002).
  - [13] I. Vidaña, D. Logoteta, C. Providência, A. Polls, and I. Bombaci, *Eur. Phys. Lett.* **94**, 11002 (2011).
  - [14] Y. Yamamoto, T. Furumoto, N. Yasutake, and T. A. Rijken, *Phys. Rev. C* **90**, 045805 (2014).
  - [15] Y. Yamamoto, T. Furumoto, N. Yasutake, and T. A. Rijken, *Eur. Phys. J. A* **52**, 19 (2016).
  - [16] Y. Yamamoto, H. Togashi, T. Tamagawa, T. Furumoto, N. Yasutake, and T. A. Rijken, *Phys. Rev. C* **96**, 065804 (2017).
  - [17] D. Lonardonì, A. Lovato, S. Gandolfi, and F. Pederiva, *Phys. Rev. Lett.* **114**, 092301 (2015).
  - [18] D. Logoteta, I. Vidaña, and I. Bombaci, *Eur. Phys. J. A* **55**, 207 (2019).
  - [19] D. Cerstung, N. Kaiser, and W. Weise, *Eur. Phys. J. A* **56**, 175 (2020).
  - [20] A. Drago, A. Lavagno, G. Pagliara, and D. Pigato, *Phys. Rev. C* **90**, 065809 (2014).
  - [21] D. B. Kaplan and A. E. Nelson, *Phys. Lett. B* **175**, 57 (1986); **179**, 409 (1986).
  - [22] G. E. Brown, C.-H. Lee, M. Rho, and V. Thorsson, *Nucl. Phys. A* **567**, 937 (1994).
  - [23] V. Thorsson, M. Prakash, and J. M. Lattimer, *Nucl. Phys. A* **572**, 693 (1994).
  - [24] C.-H. Lee, *Phys. Rep.* **275**, 255 (1996).
  - [25] N. K. Glendenning and J. Schaffner-Bielich, *Phys. Rev. Lett.* **81**, 4564 (1998).
  - [26] M. Baldo, G. F. Burgio, and H.-J. Schulze, in *Superdense QCD Matter and Compact Stars*, NATO Science Series 2:

- Mathematics, Physics and Chemistry Vol. 197, edited by D. Blaschke and D. Sedrakian (Springer, Berlin, 2006).
- [27] F. Özel, D. Psaltis, S. Ransom, P. Demorest, and M. Alford, *Astrophys. J.* **724**, L199 (2010).
- [28] I. Sagert, G. Pagliara, M. Hempel, and Schaffner-Bielich, *Astrophys. J.* **740**, L14 (2011).
- [29] T. Kühn, R. Lastowiecki, and D. Blaschke, *Phys. Rev. D* **88**, 085001 (2013).
- [30] L. Bonanno and A. Sedrakian, *Astron. Astrophysics, A&A*, **J539**, 416 (2012).
- [31] R. Lastowiecki, D. Blaschke, H. Grigorian, and S. Typel, *Acta Physica Polonica B Proceedings Supplement* **5(2)** 535 (2012).
- [32] M. Shahrabaf, D. Blaschke, A. G. Grunfeld, and H. R. Moshfegh, *Phys. Rev. C* **101**, 025807 (2020).
- [33] M. Shahrabaf, D. Blaschke, and S. Khanmohamadi, *J. Phys. G: Nucl. Part. Phys.* **47**, 115201 (2020).
- [34] K. Otto, M. Oertel, and B.-J. Schaefer, *Phys. Rev. D* **101**, 103021 (2020).
- [35] T. Kojo, G. Baym, and T. Hatsuda, *Astrophys. J.* **934**, 46 (2022).
- [36] Y. Yamamoto, N. Yasutake, and T. A. Rijken, *Phys. Rev. C* **105**, 015804 (2022).
- [37] A. Akmal, V. R. Pandharipande, and D. G. Ravenhall, *Phys. Rev. C* **58**, 1804 (1998).
- [38] M. M. Nagels, T. A. Rijken, and Y. Yamamoto, *Phys. Rev. C* **99**, 044002 (2019).
- [39] M. M. Nagels, T. A. Rijken, and Y. Yamamoto, *Phys. Rev. C* **99**, 044003 (2019).
- [40] M. M. Nagels, Th. A. Rijken, and Y. Yamamoto, *Phys. Rev. C* **102**, 054003 (2020).
- [41] L. McLerran and H. D. Pisarski, *Nucl. Phys. A* **796**, 83 (2007).
- [42] Y. Hidaka, L. McLerran, and H. D. Pisarski, *Nucl. Phys. A* **808**, 117 (2008).
- [43] L. McLerran and S. Reddy, *Phys. Rev. Lett.* **122**, 122701 (2019).
- [44] S. Han, M. A. A. Mamun, S. Lalit, C. Constantinou, and M. Prakash, *Phys. Rev. D* **100**, 103022 (2019).
- [45] D. C. Duarte, S. Hernande-Ortiz, and K. S. Jeong, *Phys. Rev. C* **102**, 025203 (2020); **102**, 065202 (2020).
- [46] T. Zhao and J. M. Lattimer, *Phys. Rev. D* **102**, 023021 (2020).
- [47] J. Margueron, H. Hansen, and P. Proust, and G. Chanfray, *Phys. Rev. C* **104**, 055803 (2021).
- [48] G. Cao, *Phys. Rev. D* **105**, 114020 (2022).
- [49] A. B. Kaidalov and K. A. Ter-Matrosian, *Nucl. Phys. B* **75**, 471 (1974).
- [50] H. Togashi and M. Takano, *Nucl. Phys. A* **902**, 53 (2013).
- [51] N. K. Glendenning, *Phys. Rev. D* **46**, 1274 (1992).
- [52] G. Baym, A. Bethe, and C. Pethick, *Nucl. Phys. A* **175**, 225 (1971).
- [53] G. Baym, C. J. Pethick, and P. Sutherland, *Astrophys. J.* **170**, 299 (1971).